Optics Communications 603 (2026) 132813

Contents lists available at ScienceDirect

Optics Communications

journal homepage: www.elsevier.com/locate/optcom

Photonic-assisted transceiver for high-frequency probe signal generation and microwave DFS measurement

Simin Li *, Zijian Yuan, Wenjun Zhao, Yu Zhang, Shilong Pan

National Key Laboratory of Microwave Photonics, Nanjing University of Aeronautics and Astronautics, Nanjing, 210016, China

ARTICLE INFO

Keywords:
Microwave photonics
Measurement
Doppler frequency shift
Transceiver

ABSTRACT

This paper presents a photonic-assisted transceiver that integrates a high-frequency probe signal generator with a microwave Doppler frequency shift (DFS) measurement receiver. The system employs photonic frequency quadrupling to generate the probe signal, which relaxes the requirements for the transmitter's microwave source. It also reuses the two high-order optical sidebands as optical carriers at the receiver, eliminating the electrical local oscillator and enabling detection with a low-frequency reference signal. Optical single-sideband modulation is applied to both the echo and reference signals, allowing the system to avoid optical filters and use a low-frequency photodetector for measuring both the amplitude and sign of the DFS. Experimental results demonstrate the generation of a 36-GHz probe signal and successful extraction of DFS within a range of −150 to +150 kHz.

1. Introduction

The fundamental significance of Doppler frequency shift (DFS) lies in deducing the relative motion state of a target through variations in frequency, which is extensively utilized in domains including radar systems, wireless communication networks, navigation, and Internet of Things applications for motion detection and environmental sensing. The magnitude of the DFS is linearly proportional to the target's velocity, while its sign (positive or negative) directly indicates the direction of motion. Therefore, the simultaneous acquisition of both amplitude and sign of the DFS is essential for the measurement systems. Furthermore, the DFS amplitude exhibits a linear positive correlation with the carrier frequency. Under identical relative velocity conditions, high-frequency signals induce significantly greater DFS amplitudes than low-frequency signals, indicating that higher probe frequencies can enhance the measurement sensitivity. Numerous electronic techniques have been proposed for the estimation of DFS; however, due to inherent electronic bottlenecks, these methods face considerable challenges when implemented at high-frequency. Over the past few years, many microwave photonic schemes have been developed to address this limitation. Most of them, the probe and echo signals are modulated onto the same optical carrier via an electro-optical modulator. By mixing the probe and echo signals, the DFS magnitude could be extracted. To estimate the DFS sign, various methods have been demonstrated, including the introduction of a frequency shift [1,2], photonic I/Q detection [3,4] and the employment of an electrical reference [5–9]. Among these, employing an electrical reference offers a straightforward and practical solution; the sign of DFS can be inferred from the beat frequency between the echo and reference signals. In Ref. [6], the probe, reference, and echo signals are modulated onto a dual-drive Mach--Zehnder modulator (DDMZM). For optical-to-electrical conversion employing a low-frequency photodetector (PD), the reference frequency must be proximate to that of the probe signal, thereby requiring the reference signal to have a relatively high frequency. To avoid the need of high-frequency reference, the probe, reference, and echo signals are modulated through cascaded modulators using optical single-sideband (OSSB) modulation or carrier-suppressed OSSB modulation techniques [7,8]. Furthermore, almost all microwave photonic DFS estimation techniques rely solely on photonic components for receiver construction, whereas a high-frequency purely electronic signal generator remains essential at the transmitter end.

This work presents a photonic-assisted transceiver that integrates a high-frequency probe signal generator with a microwave DFS measurement receiver, inspired by the architecture of microwave photonic radar systems [10] and integrated photonic chips [11]. Compared with other microwave photonic DFS measurement techniques, this approach innovatively combines the generation of high-frequency probe signals through photonic frequency quadrupling. This integration offers two

* Corresponding author.
E-mail address: lisimin@nuaa.edu.cn (S. Li).

https://doi.org/10.1016/j.optcom.2025.132813
Received 9 November 2025; Received in revised form 11 December 2025; Accepted 22 December 2025
Available online 22 December 2025

principal advantages. The first is the relaxation of high-frequency requirements for the transmitter's microwave source. The second is the reuse of the two high-order optical sidebands as optical carriers at the receiver, thereby not only eliminating the need for an electrical local oscillator (LO) but also allowing the system to perform detection using a low-frequency PD with a low-frequency reference signal. At the receiver, a dual-parallel Mach-Zehnder modulator (DPMZM) is employed to modulate both the echo signal and a low-frequency reference signal onto the two optical carriers using OSSB modulation. For a specific optical carrier (denoted as Carrier 1), the echo signal modulated onto the other carrier (Carrier 2) lies in close spectral proximity. The frequency difference between this external echo signal and Carrier 1 corresponds to the DFS component. Concurrently, Carrier 1 is also modulated with a low-frequency reference signal. Following photodetection, three distinct components are simultaneously obtained in the low-frequency band: the DFS component, a sign-discrimination component representing the beat frequency between the echo and reference signals, and the reference component itself. The OSSB modulation is essential for ensuring the scheme's feasibility. By preventing unwanted sidebands and ensuring a clean sign-discrimination component through OSSB modulation, this approach enables the use of a single low-frequency PD to determine the DFS amplitude and sign. This eliminates the need for optical filters, thereby substantially reducing system complexity and cost. This approach demonstrates significant potential for applications in domains such as integrated sensing and communication systems and autonomous vehicles [12]. The system's functionality has been validated via simulation as detailed in Ref. [13], and this work presents the experimental results of the proposed approach.

2. Principle

Fig. 1 illustrates the architecture of the photonic-assisted transceiver for microwave DFS measurement. At the transmitter, an optical carrier with a frequency of f_c from a laser diode is sent to a DPMZM. A fundamental frequency microwave signal with a frequency of f_0 is injected into the two RF ports through a 90-degree electrical hybrid coupler. The primary MZM (MZM1-c) within the DPMZM1 operates at the minimum transmission point, while the two sub-MZMs (MZM1-a & b) operate at their maximum transmission points. As a result, a carrier-suppressed even-order sideband modulation is implemented. The small-signal output of the DPMZM is characterized by

$$E_{DPMZM1} \propto J_2(\beta_1)\left\{\begin{array}{l}\exp\left[j2\pi(f_C-2f_0)t\right]\\+\exp\left[j2\pi(f_C+2f_0)t\right]\end{array}\right\} \quad (1)$$

where J_2 is the 2nd order Bessel function of the first kind, and β_1 is the modulation index. Then the ±2nd order sideband signal is divided into

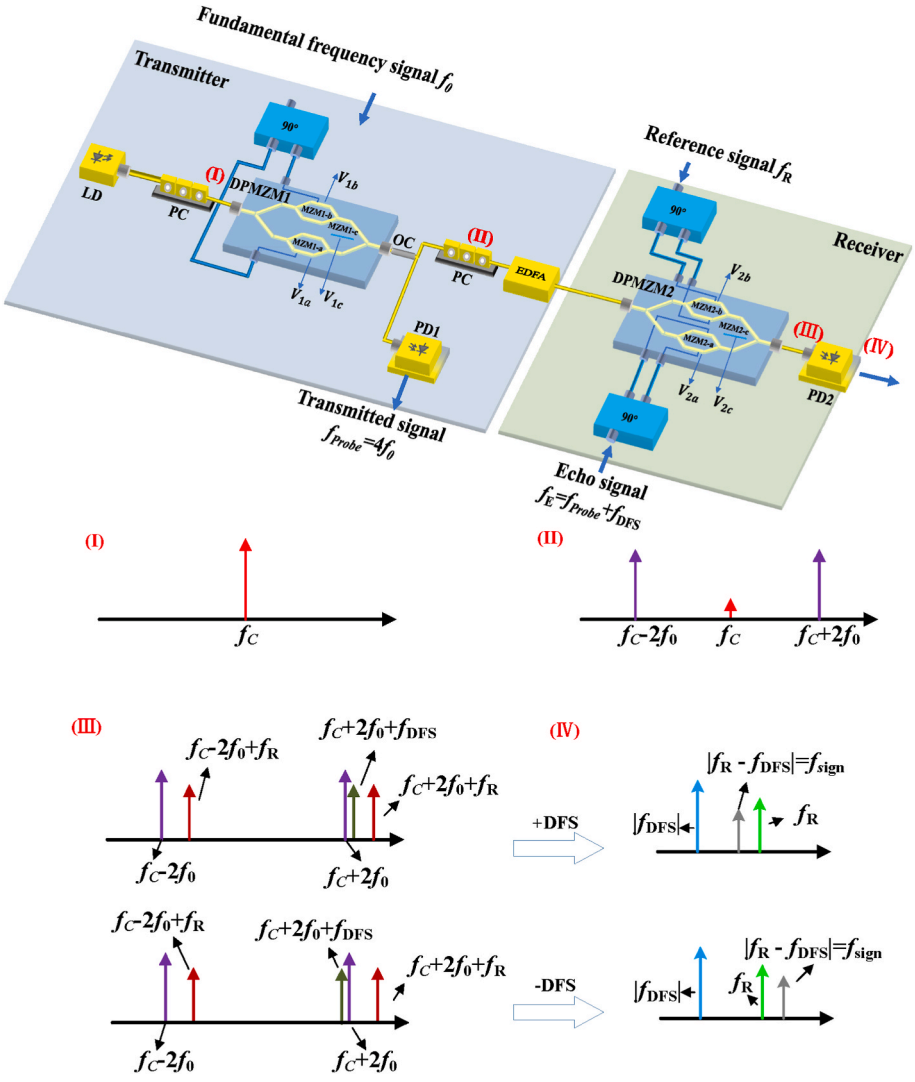

Fig. 1. Configuration of the photonic-assisted transceiver. LD: laser diode; PC: polarization controller; DPMZM: dual-parallel Mach-Zehnder modulator; OC: optical coupler; PD: photodetector; EDFA: erbium-doped fiber amplifier.

two pathways. One is fed into a PD (PD1) to produce a frequency-quadrupled probe with a frequency of $f_{Probe} = 4f_0$. The other serves as an optically transmitted LO signal for the receiver, subsequently fed into a second DPMZM (DPMZM2). Unlike DPMZM1, DPMZM2 incorporates two DDMZMs, with each sub-MZM featuring dual RF input ports on its arms. An electrical 90-degree electrical hybrid coupler applies the echo signal with $f_E = 4f_0+f_{DFS}$, where f_{DFS} denotes the frequency-shifted signal, to a sub-MZM (MZM2-a) in DPMZM2. To implement OSSB modulation, MZM2-a operates at the quadrature point by setting an appropriate DC bias V_{2a}. Similarly, a reference signal f_R is converted into an OSSB signal by the other sub-MZM (MZM2-b). Assuming the two OSSB signals contain only the +1st order sideband, the optical signal from DPMZM2 can be written as

$$\begin{aligned} E_{DPMZM2} &\propto J_2(\beta_1)J_0(\beta_2)\{\exp[j2\pi(f_C-2f_0)t]+\exp[j2\pi(f_C+2f_0)t]\} \\ &+jJ_2(\beta_1)J_1(\beta_2)\left\{\begin{array}{l}\exp[j2\pi(f_C-2f_0+f_R)t]+\exp[j2\pi(f_C+2f_0+f_R)t] \\ +\exp[j2\pi(f_C-2f_0+f_E)t]+\exp[j2\pi(f_C+2f_0+f_E)t]\end{array}\right\} \\ &\propto J_2(\beta_1)J_0(\beta_2)\{\exp[j2\pi(f_C-2f_0)t]+\exp[j2\pi(f_C+2f_0)t]\} \\ &+jJ_2(\beta_1)J_1(\beta_2)\left\{\begin{array}{l}\exp[j2\pi(f_C-2f_0+f_R)t]+\exp[j2\pi(f_C+2f_0+f_R)t] \\ +\exp[j2\pi(f_C+2f_0+f_{DFS})t]+\exp[j2\pi(f_C+6f_0+f_{DFS})t]\end{array}\right\} \end{aligned} \quad (2)$$

The optical components f_C+2f_0 and $f_C+2f_0+f_{DFS}$ exhibit closely spaced frequencies, because the frequency of the DFS, typically in the kHz to MHz range, is substantially lower than the probe frequency (~GHz or tens of GHz). By introducing a low-frequency signal f_R, where $|f_{DFS}| < f_R \ll f_{Probe}$, as illustrated in Fig. 1(III)with a frequency higher than $|f_{DFS}|$ but significantly lower than f_{Probe}, As can be seen from Fig. 1 (III), three low-frequency beat frequency components f_R, $|f_{DFS}|$ and $|f_R-f_{DFS}| = f_{sign}$ can be generated at a low-frequency PD (PD2). The value of f_R is predetermined, and $|f_{DFS}|$ is the magnitude of the DFS. According to the DFS equation, the radial velocity of the target can be calculated from $|f_{DFS}|$ as follows:

$$v = |f_{DFS}|c / 2f_{Probe}\cos\theta \quad (3)$$

where c is the speed of light in vacuum and θ denotes the antenna's elevation angle. If f_{sign} is less than f_R, the f_{DFS} is positive, indicating that the target is approaching, and vice versa. Other beat frequency components, such as those between f_C-$2f_0$ and $f_C+2f_0+f_R$, as well as f_C-$2f_0$ and $f_C+2f_0+f_{DFS}$, are much larger than the aforementioned three frequency components and remain undetected due to PD2 bandwidth limitations.

Based on the aforementioned analysis, the velocity and direction of the moving object can be effectively determined by analyzing the correlation among the three beat frequency components. This necessitates that both the echo and reference signals be modulated using the OSSB technique. If double-sideband (DSB) modulation is employed instead, the resulting unwanted sidebands would produce extraneous beat components, thereby obscuring the sign of the DFS unless a highly selective optical filter is introduced. Even in DSB modulation system with optical filtering, the use of a low-frequency reference signal leads to extremely narrow spectral separation between the unwanted sidebands and the optical carrier. This demands a filter with a sharp roll-off characteristic, which not only raises system cost but also heightens sensitivity to component tolerances, making the overall approach challenging to implement in practice.

3. Experiment setup and results

An experiment setup is established based on the configuration depicted in Fig. 1. An optical carrier at 1550.13 nm, emitted from a laser diode (Teraxion Pure Spectrum-NLL), is injected into a DPMZM (DPMZM1, Fujitsu FTM7961). A 9-GHz microwave signal with an output power of 18 dBm generated by a microwave signal generator (Anapico APMS40G-4) is applied to DPMZM1. The DC biases of DPMZM1 are carefully adjusted to realize the carrier-suppressed even-order sideband modulation.

Fig. 2 (a) presents the optical spectrum of the carrier-suppressed ±2nd order sideband optical signal observed by an optical spectrum analyzer (YOKOGAWA AQ6370D). The modulated optical signal output from the DPMZM is split into two branches via a 1 × 2 optical coupler (OC). The optical signal in the lower branch is amplified and is directed into a 40-GHz PD (Finisar XPDV2120RA) to generate a frequency-quadrupled probe signal at 36 GHz, which is observed by an electrical spectrum analyzer (ESA, KEYSIGHT, MXA Signal Analyzer), as depicted in Fig. 2 (b). A power difference of 20.9 dB is observed between the main peak and the fundamental frequency of 9 GHz.

The optical signal output from the other port of the OC is directed to a DPMZM (DPMZM2, Fujitsu FTM7960EX), which consists of two DDMZMs in the receiver. A simulated echo signal of 10 dBm is produced by a signal generator (KEYSIGHT PSG E8257D), while a microwave signal generator (Anapico APMS40G-4) generates a reference signal at 15 dBm. These RF signals are applied to the sub-MZMs within the DPMZM2 via two 90-degree electrical hybrid couplers, respectively. The frequency of the reference is set to 1 GHz, which is the lowest operating frequency of the 90-degree electrical hybrid coupler. The reference frequency could be further reduced by using a low-frequency hybrid coupler. The optical spectrum of the OSSB modulation signal is depicted in Fig. 3(a). It should be noted that the sideband of the echo is positioned extremely close to the optical carrier, rendering it indistinguishable in the figure. After amplification, the optical signal output from DPMZM2 is fed into a PD (PD2, Finisar XPDV2120RA) for optical-to-electrical conversion.

To validate the efficacy of the proposed system for simultaneously estimating both the magnitude and sign of the DFS, the echo frequency is set at 36.00015 and 35.99985 GHz, corresponding to positive DFS of +150 kHz and negative DFS of −150 kHz, respectively. Fig. 3(b) and (c) present the measured electrical spectra. Regardless of the DFS polarity, the beat frequency components are distributed across two distinct regions. The low-frequency range and high-frequency are both measured with a resolution bandwidth (RBW) of the ESA set to 36 Hz. Within the low-frequency range, a frequency component corresponding to the absolute value of the DFS is detected at 150 kHz. In the vicinity of 1 GHz, the dominant peak at 1 GHz represents the reference signal f_R, while a secondary peak corresponds to the directional discrimination signal f_{sign}. The sign of f_{DFS} can be inferred from the relationship between f_R and f_{sign}. When the DFS is positive, the echo frequency is 36.00015 GHz, resulting in f_R exceeding f_{sign}; conversely, for negative DFS, f_R is less than f_{sign}. An undesired image frequency signal f_I, primarily generated by the undesired -1st order reference sideband and the desired +1st order echo sideband, is also observed. When the DFS is +150 kHz, the power of f_I is more than 25 dB below that of f_{sign}. Similarly, for −150 kHz DFS, the power of f_I is more than 28 dB lower than that of f_{sign}. The DFS is measured in steps of 10 kHz, ranging from −150 kHz to +150 kHz. Fig. 3 (d) illustrates the measured results with a RBW of 1 Hz. The measurement errors are also depicted in the figure, which are less than ±0.2 Hz. Reducing the RBW could further decrease measurement error but would extend the measurement duration.

To analyze the effect of reference signal power, modulated carrier frequency power, and echo signal power on system performance, the power levels of f_{sign} and f_{DFS} are measured under varying signal power conditions. Firstly, under the conditions of f_E with a fixed power of 10 dBm, and f_0 power levels at 14 dBm, 16 dBm, and 18 dBm, the effect of variations in f_R power within the range of 10 dBm to 18 dBm is examined. As shown in Fig. 4(a), the measured f_{sign} power curves display maxima when the f_R power is close to 15 dBm. This phenomenon results from increased f_R power causing a shift in the DC bias point of the modulator, thereby enhancing the mirror frequency component f_I. This deviation is likely caused by an excessively high RF drive power, which drives the RF swing into the nonlinear region of the modulator transfer characteristic. To optimize the power difference between f_{sign} and f_I, it is

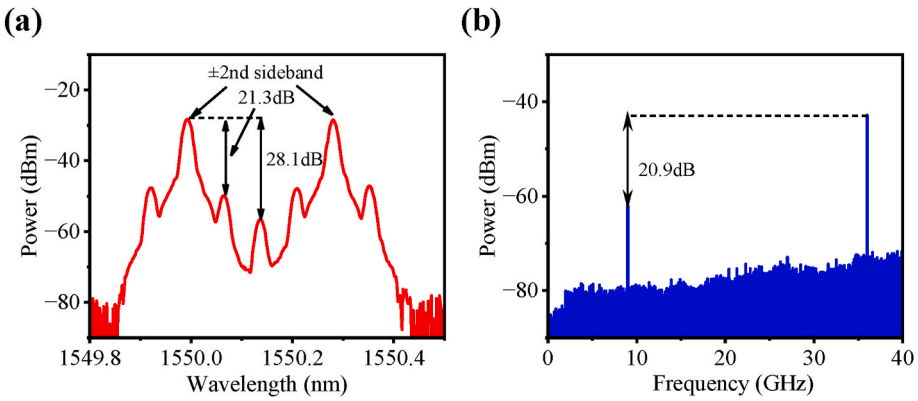

Fig. 2. (a) The optical spectrum after DPMZM1. (b) the electrical spectrum of the frequency-quadrupled probe signal.

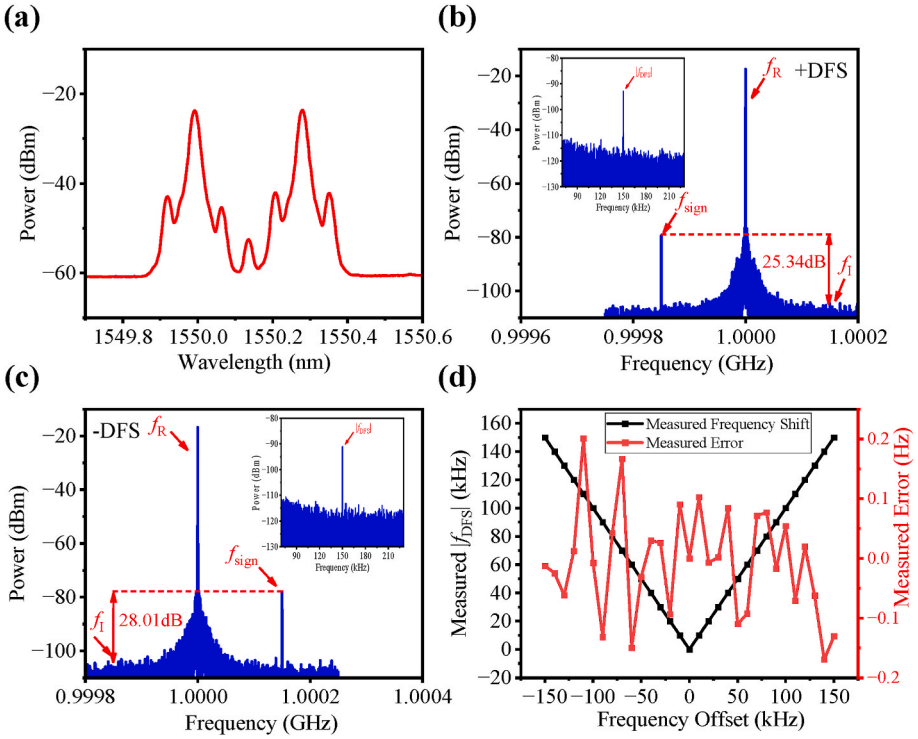

Fig. 3. (a) The optical spectrum after DPMZM2, the electrical spectra of (b) + DFS and (c) -DFS, and (d) the estimated DFSs and the measurement errors.

necessary to synchronously adjust the DC bias of DPMZM2 within the echo signal path to effectively suppress f_I. When the f_R power exceeds the optimal threshold, bias adjustment solely within the echo path becomes insufficient for complete compensation, necessitating the implementation of auxiliary bias adjustment in the reference signal path. This auxiliary adjustment leads to a reduction of f_{sign} power, thereby, resulting in a power peak of f_{sign} when f_R power is approximately 15 dBm. In practical applications, bias controllers are commonly employed to suppress such instability, while using electro-optic modulators with intrinsically low DC-drift characteristics can fundamentally resolve this issue at the device level. Possible implementation approaches include optimizing the structural design and fabrication process of thin-film lithium-niobate modulators [14], introducing magnetoelectric skyrmions [15], adopting silicon-lithium-niobate heterogeneous integration combined with silicon-waveguide-based thermal tuning for DC bias control [16], and exploring alternative material platforms such as thin-film lithium tantalate with enhanced overall properties [17].

Fig. 4(b) illustrates the effect of varying f_R power on f_{DFS} and f_{sign} under a fixed f_0 power condition of 16 dBm. The results indicate that the f_{DFS} power exhibits a decreasing trend as the f_R power increases. When the f_{sign} power reaches its optimal level at $f_R = 15$ dBm, the f_{DFS} power drops by about 1.7 dB from its maximum value. From Fig. 4 (c) and 4 (d), it is can be seen that the f_I power remains consistently below −100 dBm, maintaining a power margin exceeding 20 dB compared to the f_{sign} power, thereby eliminating the possibility of signal confusion or interference.

Fig. 5 (a) and (b) depict the effect of f_0 under different power levels. In the experiment, the power of f_E and that of f_R are fixed at 10 dBm and 15 dBm, respectively. The probe signal f_{probe}, DFS signal f_{DFS}, and sign signal f_{sign} all demonstrate an increase with rising fundamental frequency power f_0, while the interference signal power f_I exhibits minimal variation. Although when f_0 has a lower power level, f_{DFS} and f_I have comparable power levels; however, they can be readily distinguished due to their operation in different frequency bands. The findings suggest that increasing f_0 power contributes to enhancing system performance. Moreover, as shown in Fig. 5(c) and (d), when the f_0 power is 18 dBm and f_R power is 15 dBm, f_E power increases from 10 dBm to 18 dBm results in a corresponding rise in the power of the frequency components

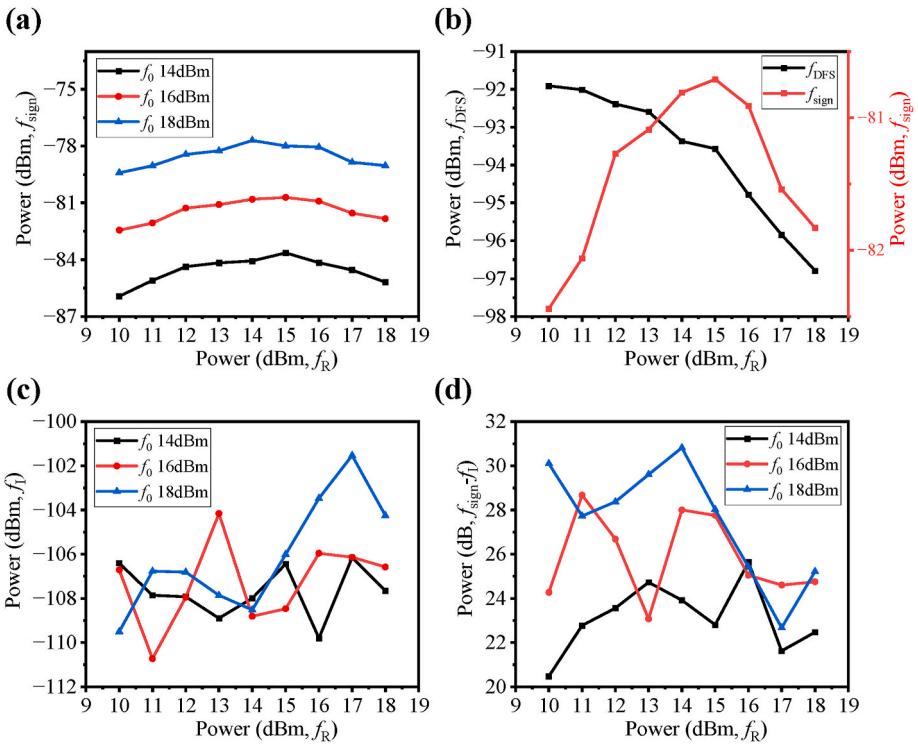

Fig. 4. The power of (a) f_{sign}, (b) f_{DFS}, (c) f_I, (d) the power difference of f_{sign} and f_I, under different power levels of f_R.

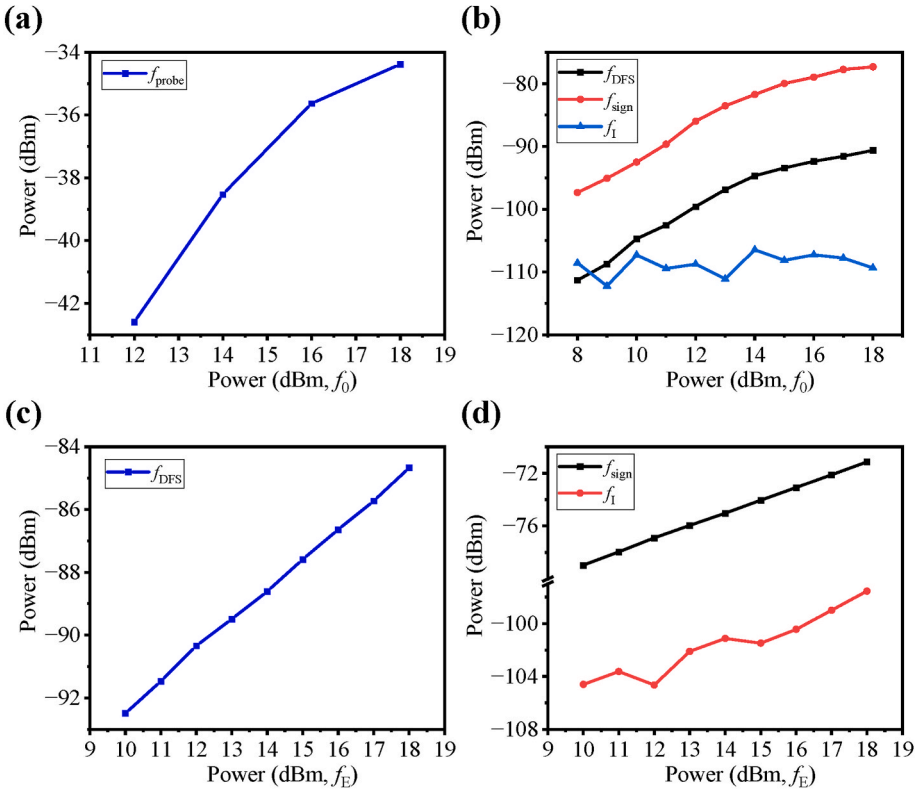

Fig. 5. The power of (a) f_{Probe}, (b) f_{DFS}, f_{sign} and f_I, under different power levels of f_0; and the power of (c) f_{DFS}, (d) f_{sign}, f_I, under different power levels of f_E.

f_{DFS}, f_{sign}, and f_I. The power difference between f_{sign} and f_I consistently remains above 25 dB. It should be noted that in practical systems, the echo signal power can be adjusted through electronic amplification.

Based on the analysis presented above, a brief comparison between this work and previously reported DFS measurement approaches is summarized in Table 1. As can be seen, the methods presented in Refs. [1–9] implement only the receiver-side functionality. The proposed method in this paper integrates both the photonic transmitter and

Table 1
Comparison of different DFS measurement schemes.

	Operating Frequency	Measured DFS Range	DFS Error	Integrated Transmitter and Receiver	Method Used	Reference Signal Frequency
Ref. [1]	6–36 GHz	−100-100 kHz	±0.15 Hz	No	Frequency shift	/
Ref. [2]	20 GHz	−100-100 kHz	±8 Hz	No		/
Ref. [3]	10 and 18 GHz	−100-100 kHz	$\pm 5 \times 10^{-3}$ Hz	No	Photonic I/Q detection	/
Ref. [4]	5–40 GHz	1–1000 kHz	±12 Hz	No		/
Ref. [5]	10, 14 and 18 GHz	−100-100 kHz	±1 Hz	No	Electrical-reference-assisted	High
Ref. [6]	12, 15 and 18 GHz	−100-100 kHz	±0.1 Hz	No		Low
Ref. [7]	6.9–16.1 GHz	−100-100 kHz	±0.04 Hz	No		Low
Ref. [8]	7–16 GHz	−100-100 kHz	±0.04 Hz	No		Low
Ref. [9]	5–30 GHz	−100-100 kHz	±0.6 Hz	No		High
This Work	36 GHz	−150-150 kHz	±0.2 Hz	Yes		Low

receiver within a single platform and utilizes a fixed low-frequency reference signal, resulting in a more compact architecture and reduced hardware complexity.

4. Conclusion

In conclusion, a transceiver integrating a high-frequency probe signal generator with a microwave DFS measurement receiver, in which both the transmitter and receiver employ photonic technologies, has been proposed and experimentally demonstrated. Through photonic frequency quadrupling, the system generates the probe signal while relaxing transmitter source requirements. The two high-order sidebands are further reused as optical carriers in the receiver, thereby eliminating the electrical LO and thus enabling detection via a low-frequency reference. In the receiver end, a DPMZM implements OSSB modulation for both the echo and reference signals, allowing a low-frequency PD to determine the DFS amplitude and sign without requiring additional optical filters. Experimental results demonstrate the generation of a 36 GHz probe signal and successful DFS extraction across ±150 kHz with measurement errors below ±0.2 Hz. Furthermore, the system's performance has been systematically characterized with respect to fundamental signal power, reference signal power, and echo signal power.

CRediT authorship contribution statement

Simin Li: Writing – review & editing, Writing – original draft, Resources, Methodology, Conceptualization. **Zijian Yuan:** Writing – review & editing, Visualization, Validation, Investigation, Data curation. **Wenjun Zhao:** Investigation. **Yu Zhang:** Writing – review & editing. **Shilong Pan:** Resources, Funding acquisition.

Disclosures

The authors declare no conflicts of interest.

Funding

The Research Fund of Microwave Photonics Technology Laboratory (2024-04).

Declaration of competing interest

The authors declare that they have no known competing financial interests or personal relationships that could have appeared to influence the work reported in this paper.

Data availability

Data underlying the results presented in this paper are not publicly available at this time but may be obtained from the authors upon reasonable request.

References

[1] Y. Gao, R. Wang, B. Kang, et al., Wideband anti-interference microwave photonic measurement for doppler frequency shift and angle of arrival, IEEE Trans. Instrum. Meas. 73 (2024) 1–8.
[2] M. Jiao, L. Li, Y. Jiang, et al., Photonic scheme for the simultaneous measurement of doppler frequency shift and angle of arrival based on optical frequency shift heterodyne and power mapping, Opt. Express 32 (22) (2024) 39950–39962.
[3] P. Li, L. Yan, J. Ye, et al., Photonic approach for simultaneous measurements of doppler-frequency-shift and angle-of-arrival of microwave signals, Opt. Express 27 (6) (2019) 8709–8716.
[4] F. Zhang, J. Shi, S. Pan, Photonics-based wideband doppler frequency shift measurement by in-phase and quadrature detection, Electron. Lett. 54 (11) (2018) 708–710.
[5] L. Xu, Y. Yu, H. Tang, et al., A simplified photonic approach to measuring the microwave doppler frequency shift, IEEE Photon. Technol. Lett. 30 (3) (2017) 246–249.
[6] C. Huang, E.H.W. Chan, C.B. Albert, et al., Wideband DFS measurement using a low-frequency reference signal, IEEE Photon. Technol. Lett. 31 (20) (2019) 1643–1646.
[7] Y. Chen, P. Zuo, T. Shi, et al., Photonic-enabled Doppler frequency shift measurement for weak echo signals based on optical single-sideband mixing using a fixed low-frequency reference, J. Lightwave Technol. 39 (10) (2021) 3121–3129.
[8] P. Zuo, Y. Chen, Photonic-assisted filter-free microwave Doppler frequency shift measurement using a fixed low-frequency reference signal, J. Lightwave Technol. 38 (16) (2020) 4333–4340.
[9] J. Tao, X. Li, R. Li, et al., Thin-film lithium niobate dual-parallel Mach-Zehnder modulator for a simple photonic system measuring Doppler frequency shift, Chin. Opt Lett. 22 (9) (2024) 090005.
[10] F. Zhang, Q. Guo, Z. Wang, et al., Photonics-based broadband radar for high-resolution and real-time inverse synthetic aperture imaging, Opt. Express 25 (14) (2017) 16274–16281.
[11] S. Li, Z. Cui, X. Ye, et al., Chip-based microwave-photonic radar for high-resolution imaging, Laser Photon. Rev. 14 (10) (2020) 1900239.
[12] L. Wang, X. Wang, S. Pan, Microwave photonics empowered integrated sensing and communication for 6G, IEEE Trans. Microw. Theor. Tech. 73 (8) (2025) 5295–5315.
[13] W. Zhao, X. Yao, C. Yu, et al., A photonic-assisted transceiver for microwave Doppler frequency shift measurement, Proc. SPIE 11902 (2021) 58–61.
[14] M. Yeh M, D. Barton D, G Smith, et al. Interface-mediated dc electro-optic instability in lithium niobate nanophotonics, preprint, https://doi.org/10.21203/rs.3.rs-5775859/v1.
[15] T. Chu, Y. Yu, B. Xiong, et al. Room-temperature magnetoelectrical skyrmions in $LiNbO_3$ with suppressed DC drift and enhanced Eeectro-optic functionality, preprint, https://doi.org/10.21203/rs.3.rs-7303233/v1.
[16] S. Sun, M. He, M. Xu, et al., Bias-drift-free Mach-Zehnder modulators based on a heterogeneous silicon and lithium niobate platform, Photonics Res. 8 (12) (2020) 1958–1963.
[17] C. Wang, D. Fang, J. Zhang, et al., Ultrabroadband thin-film lithium tantalate modulator for high-speed communications, Optica 211 (12) (2024) 1614–1620.